Materials & Design 265 (2026) 115912

Contents lists available at ScienceDirect

Materials & Design

journal homepage: www.elsevier.com/locate/matdes

Optimizing Sb_2Se_3 solar cells with $CdIn_2S_4$ buffer for high-efficiency and stability: a comprehensive analysis

Danial Keighobadi [a], Mehdi Mousavi-Kamazani [b], Mohammad Danaie [a,*]

[a] Faculty of Electrical and Computer Engineering, Semnan University, Semnan, Iran
[b] Department of Nanotechnology, Faculty of New Sciences and Technologies, Semnan University, Semnan, Iran

ARTICLE INFO

Keywords:
Solar Cell
Sb_2Se_3
$Cdln_2S_4$
InterfacialBand Engineering

ABSTRACT

The long-standing dependence of *Sb2Se3* thin-film photovoltaics on *CdS* buffer layers continues to hinder device scalability due to parasitic UV absorption and unfavorable interface band energy. In this work, a simulation-guided interfacial engineering strategy is established by replacing *CdS* with *CdIn2S4* buffer layer. SCAPS-1D calculations demonstrate that *CdIn2S4* simultaneously increases the built-in electric field and suppresses defect-mediated interfacial recombination, leading to a significant enhancement in the open-circuit voltage (from 0.48 to 0.77 V), short-circuit current density (from 30.87 to 34.18 $mA{\cdot}cm^{-2}$), fill factor (from 67.8 to 72.16%), and overall efficiency (from 10.12% to 19.06%). Mott–Schottky analysis reveals a substantial improvement in the depletion region with an elevated built-in potential (from 0.78 to 1.05 V), whereas impedance spectroscopy indicates reduced recombination resistance and enhanced carrier extraction dynamics. These electronic improvements are coupled with the optical benefits of *CdIn2S4*, whose wide bandgap (2.6 eV) reduces parasitic absorption and increases UV photon utilization. Furthermore, the material's thermochemical formation pathway in spray pyrolysis, governed by thiourea-derived sulfur release, ensures defect-tolerant growth and chemical compatibility with *Sb2Se3*. This combined physicochemical–optoelectronic synergy positions *CdIn2S4* as a viable industrial alternative to *CdS*, offering a scalable pathway toward high-efficiency, environmentally friendly *Sb2Se3* photovoltaics.

1. Introduction

With increasing concerns for climate change and the need to reduce greenhouse gas emissions, the focus on renewable energy sources, particularly solar energy, has grown significantly in recent years. Solar energy, as one of the most sustainable energy sources, offers numerous advantages in mitigating dependence on fossil fuels. One of the main challenges for the wider adoption of solar energy is the development of economically viable and efficient photovoltaic (PV) technologies. Thin-film solar cells, due to their low fabrication costs, compatibility with flexible substrates, and scalability for large-area production, have attracted considerable attention [1–5].

In recent years, *Sb2Se3* has emerged as a promising absorber material for thin-film solar cells. This material offers key advantages such as one-dimensional ribbon-like structure, high carrier mobility, strong optical absorption ($>10^5 cm^{-1}$), and optimal bandgap (1.1–1.2 eV), making it a superior alternative to traditional materials like silicon. Despite the promising properties of *Sb2Se3*, its solar cell performance is still limited by challenges such as carrier recombination and band misalignment at the absorber-buffer interface [1,6–8].

One of the key components in solar cell structures is the use of buffer layers to improve the interface between the absorber material and the electron transport layer (ETL). *CdS* has traditionally been used as a buffer layer in *Sb2Se3*-based devices. However, CdS poses several issues, including significant parasitic absorption below 520 nm, and poor band alignment with *Sb2Se3*, leading to carrier recombination at the interface and reduced cell performance [9–13]. Due to the issues associated with *CdS*, there is a growing need for wide-bandgap buffer layers that can improve the efficiency of solar cells. *CdIn2S4*, a wide bandgap (2.6 eV) and optimal band alignment with *Sb2Se3*, has emerged as a potential alternative to *CdS*. *CdIn2S4* offers several advantages, including high chemical stability, low parasitic absorption, and improved photon utilization in the UV region, making it a suitable candidate for use as a buffer layer in Sb_2Se_3-based solar cells [13–17].

The proposed device architecture employs *Sb2Se3* as the absorber layer and *CdIn2S4* as the buffer layer, with *ZnO* and Al-doped *ZnO*(*AZO*)

* Corresponding author.
E-mail addresses: Danial.und@semnan.ac.ir (D. Keighobadi), m.mousavi@semnan.ac.ir (M. Mousavi-Kamazani), danaie@semnan.ac.ir (M. Danaie).

https://doi.org/10.1016/j.matdes.2026.115912
Received 13 December 2025; Received in revised form 6 February 2026; Accepted 23 March 2026
Available online 29 March 2026

serving as the electron transport layer and transparent conductive oxide (TCO), respectively. The introduction of *CdIn2S4* provides a wider bandgap and more favorable band alignment with *Sb2Se3*, which enhances carrier selectivity at the heterointerface and suppresses interfacial recombination [18,19].

The *ZnO* and *AZO* layers primarily function as electron-selective transport and current-collecting layers, benefiting from their high electrical conductivity and excellent optical transparency. These properties facilitate efficient carrier extraction and low optical loss while maintaining compatibility with low-cost and scalable fabrication processes [20,21].

CdIn2S4 is a spinel-structured semiconductor with the chemical formula *CdIn2S4* that has garnered attention as a promising material for buffer layers in thin-film solar cells. The crystal structure of *CdIn2S4* is of the spinel type, and it functions as an n-type semiconductor. In this structure, cadmium (Cd^{2+}) cations occupy the tetrahedral (A-site) positions, while indium (In^{3+}) cations occupy the octahedral (B-site) positions. The sulfur (S^{2-}) anions are arranged in a regular network between these metal cations [22–27].

The *CdIn2S4* spinel structure has a low defect density, making it an excellent material for optical and electrical applications. One of the most significant features of *CdIn2S4* is its wide bandgap (2.6 eV), which makes it highly transparent in the UV region and reduces parasitic absorption. This wide bandgap allows lighter to pass through the buffer layer and reach the *Sb2Se3* absorber, improving overall photon utilization in the solar cell. Additionally, the spinel structure of *CdIn2S4* enables it to effectively suppress trap states near the conduction and valence band edges, reducing interface recombination and enhancing charge carrier extraction [28–32].

The chemical and structural properties of *CdIn2S4* make it an ideal alternative to *CdS* in *Sb2Se3*-based solar cells, as it not only reduces parasitic absorption but also improves band alignment with the absorber layer. These characteristics contribute to higher photovoltaic efficiency and device stability [33]. It should be noted that the lower defect density associated with the *Sb2Se3*/*CdIn2S4* interface is not assumed as an intrinsic material constant. Instead, it is inferred from a combination of literature reports on *CdIn2S4* buffer layers and the quantitative consistency between simulation results, defect sensitivity analysis, and the built-in potential extracted from Mott–Schottky characteristics. The reduced effective interface defect density required to reproduce the observed device performance further supports this interpretation [14,34–37].

The primary objective of this study is to investigate and evaluate the performance of thin-film solar cells using the absorber material *Sb2Se3* and the *CdIn2S4* buffer layer, which is considered as a replacement for *CdS*. Specifically, this study focuses on the impact of *CdIn2S4* as the buffer layer in enhancing the electrical and optical performance of the *Sb2Se3*/*CdIn2S4*/*ZnO*/*Al* : *ZnO* solar cell structure. This paper primarily targets the increase in efficiency of the solar cell from 10.12% to 19.06% through the improvement of the built-in potential (V_{bi}), reduction of carrier recombination, and enhanced UV photon utilization. In this study, we specifically explore how *CdIn2S4*, a wider bandgap, can effectively address the issues associated with CdS and improve photovoltaic efficiency. We highlight that *CdIn2S4* not only reduces parasitic absorption in the UV region but also improves band alignment with *Sb2Se3*, thereby enhancing electron transfer and reducing carrier recombination at the interface.

Another critical aspect of this research is the simulation and validation of the simulation results using experimental data. The study utilizes the SCAPS-1D software to model the proposed structure and compares the simulation results with experimental data, which confirms the accuracy of the simulation model and demonstrates the predictive capability of the model in real-world conditions. The commercialization potential of this study is also of significant importance. The *Sb2Se3*/*CdIn2S4*/*ZnO*/*Al* : *ZnO* solar cells, due to their high chemical stability, low production costs, and high efficiency, offer a viable option for large-scale production and can serve as an alternative to CdS-based solar cells. [38–41]. Ultimately, this paper comprehensively investigates the potential of *Sb2Se3*-based thin-film solar technologies and the replacement of traditional buffer layers with *CdIn2S4*, aiming to achieve higher efficiency and long-term stability. It offers new pathways to enhance solar cell performance.

2. The proposed structure

Fig. 1 presents the topologies associated with the conventional and the proposed structures. As seen in (Fig. 1(a)), the reference device architecture [5] follows the conventional *Sb2Se3* thin-film solar cell configuration comprising a *Mo* back contact, a *MoSe2* interfacial layer, a Sb2Se3 absorber, a *CdS* buffer layer, a *ZnO* window layer, and an Al-doped *ZnO* (*AZO*) transparent conductive oxide capped with a metallic Au current-collecting electrodes. This structure has been widely adopted due to the favorable band alignment between *Sb2Se3* and *CdS* and the relatively low interface recombination obtained through the Mo/MoSe2 back-surface field. Despite these advantages, *CdS* imposes significant parasitic absorption in the UV–blue spectral region and introduces lattice mismatch–induced interface defects. As a result, the reference structure commonly suffers from limited short-circuit current density (J_{sc}) and a moderate open-circuit voltage (V_{oc}), which is reflected in its measured power conversion efficiency (PCE) of 10.12%.

The proposed structure (Fig. 1(b)) replaces the *CdS* buffer with a high-performance *CdIn2S4* spinel semiconductor, while preserving the overall device sequence of *Mo*/*MoSe2*/*Sb2Se3*/*ZnO*/*AZO*/*Au*. *CdIn2S4* provides several key improvements, including a wider optical bandgap (2.6 eV), substantially higher absorption coefficient in the UV-blue region, reduced parasitic loss, and superior band alignment with the *Sb2Se3* absorber. In particular, the conduction band edge of *CdIn2S4* forms a more favorable spike-type junction with Sb_2Se_3, which suppresses interface recombination and enhances carrier selectivity. Additionally, its spinel structure yields lower defect density and reduced dangling-bond formation at the heterointerface. Collectively, these factors significantly improve the photogeneration rate, carrier extraction efficiency, and junction quality compared to the *CdS*-based device.

As a direct result of these material and interfacial enhancements, the proposed *CdS*-buffered structure demonstrates a remarkable efficiency improvement from 10.12% [5] to 19.06%. The enhancement primarily originates from (i) an increase in J_{sc} due to reduced parasitic absorption and enhanced spectral response, (ii) an increase in V_{oc} arising from lower interface recombination and a more favorable conduction-band offset, and (iii) an improvement in fill factor (FF) due to reduced series resistance and improved charge transport across the heterojunction. These combined effects verify that substituting *CdS* with *CdIn2S4* is a highly effective strategy for optimizing both optical and electrical processes in *Sb2Se3* thin-film photovoltaics. The substantial performance jump confirms the strong potential of CIS-buffered *Sb2Se3* solar cells as a next-generation architecture for high-efficiency, and earth-abundant thin-film technologies.

3. Calibration and validation

All numerical simulations in this work were performed using the SCAPS-1D solar cell simulation software, which self-consistently solves the coupled Poisson and continuity equations under steady-state conditions. Standard physical models implemented in SCAPS-1D were employed to ensure consistency with established thin-film solar cell simulations.

Carrier recombination in the device was modeled by considering Shockley–Read–Hall (SRH) recombination through bulk and interface defect states, along with radiative and Auger recombination mechanisms. SRH recombination was treated as the dominant loss pathway in both the absorber and buffer layers, consistent with previous reports on

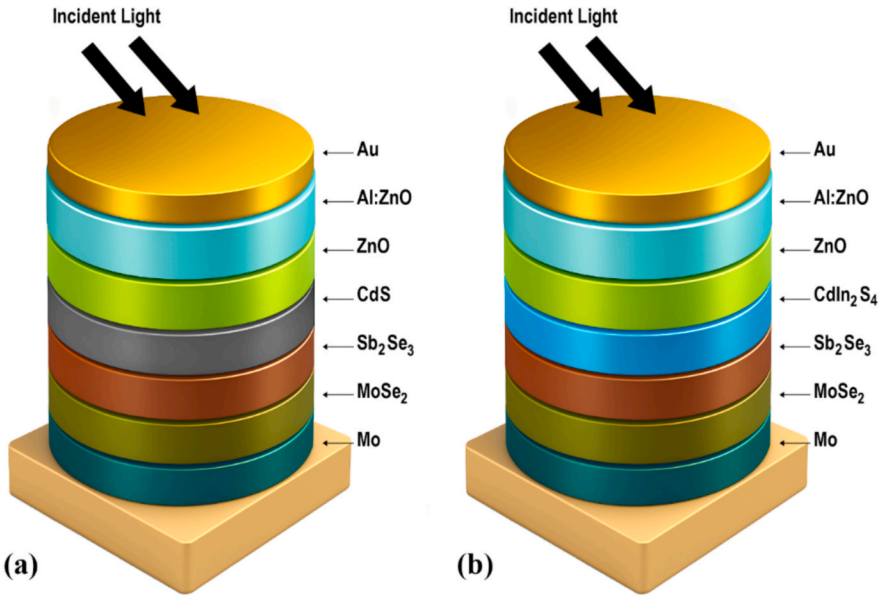

Fig. 1. (a) Schematic illustration of the reference *Sb2Se3* thin-film solar cell architecture (*Mo*/*MoSe2*/*Sb2Se3*/*CdS*/*ZnO*/*AZO*/*Au*) [5], demonstrating the conventional device structure yielding a power conversion efficiency of 10.12%. (b), Schematic illustration of the proposed high-performance architecture in which *CdS* is replaced with *CdIn2S4*(*Mo*/*MoSe2*/*Sb2Se3*/*CdIn2S4*/*ZnO*/*AZO*/*Au*), resulting in a significantly enhanced PCE of 19.06%.

Sb_2Se_3-based thin-film solar cells. Radiative and Auger recombination were included using the default SCAPS formulations to account for high-injection and band-to-band recombination effects.

Bulk defect densities for *Sb2Se3* and the buffer layers were selected based on reported experimental and simulation studies in the literature, ensuring physically realistic values. For the newly introduced *Sb2Se3*/*CdIn2S4* interface, the interface defect density was systematically varied to evaluate its impact on device performance, as presented in the Results and Discussion section. The chosen baseline interface defect density reflects a moderately optimized interface, consistent with achievable

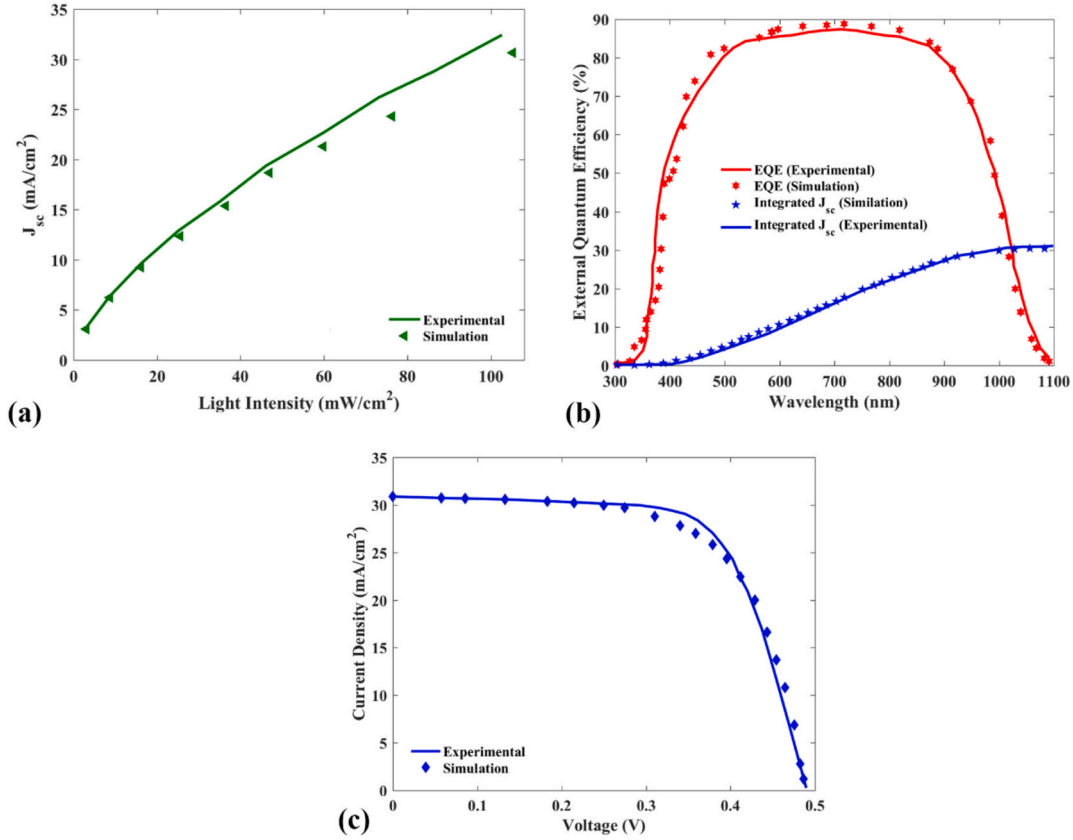

Fig. 2. (a) Comparison of short-circuit current density (J_{sc}) as a function of light intensity for simulation and experimental data. (b) Comparison of External Quantum Efficiency (EQE) and J_{sc} as a function of wavelength for simulation and experimental data. (c) Comparison of Current-Voltage (J-V) curves for simulation and experimental data [5].

values reported for chalcogenide-based heterojunctions.

Temperature-dependent simulations were conducted by varying the device temperature from 280 K to 320 K, while keeping all other parameters constant. The temperature dependence of carrier statistics, recombination rates, and transport properties was handled internally by SCAPS-1D using its built-in temperature models. This approach allowed for a consistent evaluation of the electrical response and capacitive behavior under different operating temperatures.

All simulations were performed under standard AM1.5G illumination with an incident power density of 100 $mWcm^{-2}$, assuming uniform illumination across the device area. Optical generation profiles were calculated using the absorption coefficients defined for each layer, and reflection losses were neglected, as commonly assumed in SCAPS-based simulations.

Further details regarding the numerical methods and physical models can be found in the SCAPS-1D user manual and related literature.

In this study, the photovoltaic performance of the proposed $Sb2Se3/CdIn2S4/ZnO/Al:ZnO$ architecture was numerically investigated to evaluate the impact of replacing the conventional *CdS* buffer layer with $CdIn2S4$. The analysis focuses on the coupled optical and electrical behavior of the multilayer thin-film structure, enabling a systematic assessment of charge transport, recombination processes, and overall device performance.

To verify the reliability of the numerical approach, the simulated results were calibrated and validated against reported experimental data. Three key characteristics were employed to assess the agreement between simulation and experiment, as discussed in the following section.

Fig. 2(a) depicts the short-circuit current density (J_{sc}) vs. light intensity. This plot compares our simulation data with the experimental results reported in [5]. As shown, the simulation results are in good agreement with the experimental data, confirming the high accuracy of the model. The external Quantum Efficiency (EQE) and the integrated J_{sc} as a function of wavelength are presented in Fig. 2(b). This plot demonstrates the performance of the proposed structure in light absorption and photon-to-current conversion across various wavelengths. The simulation and experimental results align well. Fig. 2(c) shows the current-Voltage (J-V) curves. The resemblance of the curves demonstrates the reliability of the simulation model.

For the structure presented in this paper, the simulation results show a significant increase in solar cell efficiency from 10.12% to 19.06% due to the use of $CdIn2S4$ as the buffer layer. This improvement is attributed to the increase in built-in potential (V_{bi}), reduced carrier recombination, and enhanced UV photon utilization. The simulations also reveal that the $CdIn2S4$ layer, with its wider bandgap, effectively reduces parasitic absorption in the UV region, leading to improved External Quantum Efficiency (EQE). Additionally, the Integrated Jsc has been increased in the proposed structure, indicating better photovoltaic performance.

Table 1 presents a comparison of the physical and electrical parameters for various thin-film solar cell structures, including Sb^2Se^3, $CdIn^2S^4$, $CdS, ZnO, ZnO-Al$, and $MoSe2$. It includes parameters such as layer thickness, bandgap (E_g), carrier concentration (N_C and N_V), carrier mobility (μ_e and μ_h), and doping concentration for each structure. A key observation from this table is the lower electron and hole mobilities in $CdIn2S4$ compared to *CdS*, attributed to its more complex crystalline structure and higher defect density. This characteristic contributes to reduced carrier recombination and enhanced charge separation efficiency, which ultimately leads to improved stability over time. Additionally, the wider bandgap of $CdIn2S4$ results in lower photon absorption in the visible range, allowing more photons to pass through to the absorber layer, which enhances solar cell efficiency.

The simultaneous use of *ZnO* and Al:*ZnO* in the proposed structure provides significant advantages that enhance the overall solar cell performance. *ZnO*, with an electron mobility of 100 $cm^2/V{\cdot}s$ and a carrier concentration of $2.2 \times 10^{18} cm^{-3}$, serves as the primary electron transport layer, and its high optical transparency allows more photons to reach the absorber layer. Meanwhile, *Al:ZnO*, with the same electron mobility of 100 $cm^2/V{\cdot}s$ and carrier concentration, benefits from aluminum doping, which improves electrical conductivity, reduces shunt resistance (R_{sh}), and enhances charge extraction efficiency. This combination of both layers results in lower charge transfer resistance (R_{ct}), leading to better overall performance. Therefore, the use of *ZnO* and *Al:ZnO* together improves carrier transport and reduces energy losses, resulting in higher efficiency and long-term stability for the solar cell.

Table 1
Comparison of material and electrical parameters for proposed and the reference solar cell structures [5].

Parameter	$Sb2Se3$	$CdIn2S4$	*CdS*	*ZnO*	*ZnO-Al*
Thickness (μm)	2.6	0.06	0.06	0.1	0.3
Eg (eV)	1.1	2.6	2.42	3.3	3.6
χe (eV)	4.16	4.1	4.45	4.5	4.5
εr	18.9	18.9	10	9	9
$N_c(1/cm^3)$	1×10^{19}	2.2×10^{18}	2.2×10^{18}	2.2×10^{18}	2.2×10^{18}
$N_V(1/cm^3)$	1×10^{19}	1.8×10^{19}	1.8×10^{19}	1.8×10^{19}	1.8×10^{19}
$\mu_e(cm^2/V{\cdot}s)$	15	10	100	100	100
$\mu_h(cm^2/V{\cdot}s)$	5.1	2	25	25	25
Doping ($1/cm^3$)	6.9×10^{15}	7.2×10^{17}	7.12×10^{17}	1×10^{18}	1×10^{20}
Function	Absorber	Buffer	Buffer	ETL	TCO/ETL

4. Simulation results and discussions

Fig. 3(a), compares the simulated energy-band diagrams of the reference device [5] and the proposed architecture, emphasizing differences in band alignment and built-in potential at the $Sb2Se3$/buffer interface. In the reference $Sb2Se3/CdS$ structure, an unfavorable conduction-band-offset (negative CBO) is formed, which promotes electron accumulation at the interface and enhances interfacial recombination, thereby limiting efficient electron extraction toward the *ZnO* layer and degrading device performance [42].

The conduction-band-offset is quantified by the conduction band offset (CBO) defined as [43]:

$$E_{\mathrm{CBO}} = E_C(\mathrm{Sb_2Se_3}) - E_C(\mathrm{CdS}) \tag{1}$$

In contrast, replacing *CdS* with $CdIn2S4$ effectively mitigates this unfavorable alignment, resulting in a near-optimal or weak spike-type CBO at the $Sb2Se3/CdIn2S4$ interface. This improved band alignment enhances electron selectivity, suppresses interfacial recombination, and increases the effective built-in potential, directly contributing to the observed improvements in V_{oc}, carrier extraction, and overall device performance.

Replacing *CdS* with $CdIn2S4$ in the proposed architecture results in a markedly improved band alignment at the $Sb2Se3$/buffer interface. This modification effectively suppresses the unfavorable conduction-band-offset present in the reference device, leading to an increased built-in potential and reduced carrier accumulation at the heterointerface. Consequently, interfacial recombination losses are significantly suppressed [44].

The optimized band alignment enables more efficient electron extraction from the $Sb2Se3$ absorber toward the *ZnO* layer, minimizing interfacial energy losses and enhancing charge collection. These improvements are directly reflected in the increased short-circuit current density and overall photovoltaic performance observed for the proposed device, confirming the critical role of $CdIn2S4$ in mitigating recombination and improving carrier transport.

The improved band alignment and the suppression of the

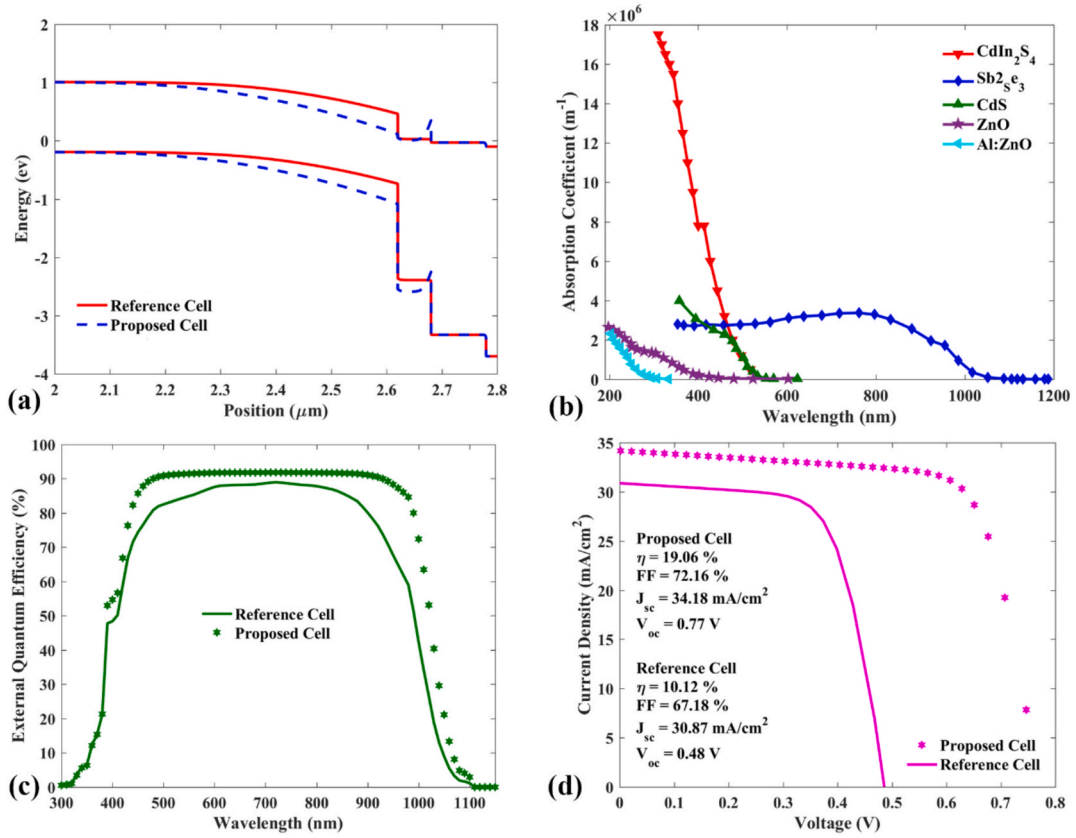

Fig. 3. (a), Simulated energy-band diagrams of the reference *Sb2Se3/CdS* [5] and proposed *Sb2Se3/CdIn2S4* devices, showing band alignment and conduction-band offsets. The proposed structure exhibits a small positive CBO (~0.2–0.3 eV), suppressing interfacial recombination. (b), Absorption coefficient spectra, indicating reduced parasitic absorption in *CdIn2S4* and enhanced photon transmission to *Sb2Se3*. (c), Simulated EQE and integrated J_{sc}, demonstrating improved spectral response across 400–1100 nm. (d), J–V characteristics under AM1.5G illumination, highlighting enhanced J_{sc}, V_{oc}, and FF in the proposed device.

conduction-band-offset in the proposed structure significantly enhance electron transfer from Sb_2Se_3 toward the *ZnO* layer, leading to an increase in J_{sc} and overall device efficiency [45,46]. This improvement is closely associated with an increased built-in potential, which strengthens the internal electric field across the heterojunction and suppresses carrier recombination at the interface. As a result, more efficient charge separation and reduced interfacial losses are achieved, directly contributing to the enhanced photovoltaic performance of the *Sb2Se3/CdIn2S4* device.

Fig. 3(b) shows the absorption coefficient spectra of the constituent layers, including *CdIn2S4*, *Sb2Se3*, *CdS, ZnO,* and *Al:ZnO,* highlighting clear differences in their optical responses across the spectral range. Notably, $CdIn_2S_4$ exhibits strong absorption in the ultraviolet region ($\lambda < 400$ nm) while remaining largely transparent in the visible range. Compared to *CdS*, this behavior significantly reduces parasitic absorption in the buffer layer.

As a result, in the proposed structure employing *CdIn2S4*, a larger fraction of incident photons is transmitted toward the Sb_2Se_3 absorber, leading to enhanced photogeneration and an increase in short-circuit current density (J_{sc}). In contrast, the reference *CdS*-based structure suffers from higher parasitic absorption, which limits photon utilization and reduces current generation.

The photon absorption rate can be expressed as [47]:

$$I_{\text{photon}} = \int_0^{\infty} \alpha(E)\,\Phi(E)\,dE \tag{2}$$

Accordingly, the higher absorption coefficient of *CdIn2S4* in the ultraviolet region increases the effective photon absorption, which directly contributes to improved current generation and overall device efficiency. These results demonstrate that substituting *CdS* with *CdIn2S4* not only improves electronic properties but also optimizes light harvesting in the proposed solar cell architecture.

Fig. 3(c) compares the external quantum efficiency (EQE) spectra of the reference device and the proposed structure as a function of wavelength. In the reference cell employing *CdS* as the buffer layer, the EQE response in the ultraviolet region is relatively low due to parasitic absorption losses in the *CdS* layer, which limit the number of photons reaching the Sb_2Se_3 absorber and reduce the photocurrent contribution at short wavelengths [48].

In contrast, the proposed structure exhibits a clear enhancement in EQE in the UV region. This improvement arises from the reduced parasitic absorption and improved optical transparency of *CdIn2S4*, which allows more photons to reach the absorber and enhances photon-to-electron conversion. Consequently, the increased EQE directly contributes to a higher short-circuit current density and overall photovoltaic efficiency in the proposed device [49,50].

In the proposed structure, the increase in photon absorption in the UV region leads to higher short-circuit current (J_{sc}) and enhanced solar cell efficiency.

Fig. 3(d), illustrates the Current-Voltage (J-V) curve for the reference cell and the proposed cell. This diagram provides a comprehensive comparison between the two structures, specifically analyzing the performance of the solar cells in terms of short-circuit current (J_{sc}), open-circuit voltage (V_{oc}), fill factor (FF), and solar cell efficiency (η). The comparison clearly shows that the proposed structure outperforms the reference structure.

For our structure, the short-circuit current (J_{sc}) reaches 34.18 mA/cm^2, which is about 10% higher than in the reference structure (30.87 mA/cm^2). This increase in Jsc is due to the improved photon absorption in the proposed structure, particularly in the UV region, and the

optimized transfer of electrons to the absorber layer (*Sb2Se3*). This enhanced photon absorption in *CdIn2S4*(buffer layer) allows more photons to enter the solar cell, resulting in increased short-circuit current (J_{sc}).

Another critical parameter in solar cell performance analysis is the open-circuit voltage (V_{oc}). In the proposed structure, Voc reaches 0.77 V, which is 0.29 V higher than in the reference structure (0.48 V). This increase in V_{oc} indicates a higher built-in potential and reduced carrier recombination at the interfaces. These characteristics lead to increased stability and reduced energy losses.

The J–V characteristics reveal a clear performance enhancement in the proposed device compared to the reference structure. Notably, the fill factor (FF) increases from 67.18% in the reference cell to 72.16% in the proposed device, indicating reduced electrical losses and improved charge transport resulting from optimized band alignment and lower internal resistance [51,52].

The most significant outcome derived from the J–V analysis is the substantial improvement in power conversion efficiency. The proposed structure achieves an efficiency of 19.06%, more than doubling that of the reference device (10.12%). This enhancement originates from the simultaneous improvement of short-circuit current density, open-circuit voltage, and fill factor, reflecting more effective photon utilization, suppressed interfacial recombination, and improved carrier extraction in the *CdIn2S4*-based architecture[53,54].

Overall performance metrics clearly demonstrate the superiority of the proposed architecture over the reference device. The short-circuit current density in the proposed structure is approximately 10% higher than that of the reference device, reflecting improved photon utilization and more efficient charge extraction enabled by the optimized buffer layer.

In addition, the open-circuit voltage increases by 0.29 V in the proposed structure, indicating a higher effective built-in potential and suppressed interfacial recombination. The fill factor is also significantly enhanced, reaching 72.16% compared to 67.18% in the reference cell, which points to reduced electrical losses and improved charge transport.

As a result of these combined improvements, the power conversion efficiency of the proposed device reaches 19.06%, more than doubling the efficiency of the reference structure (10.12%).

The efficiency enhancement observed in the proposed *Sb2Se3*/*CdIn2S4* device arises from a well-defined sequence of interrelated physical mechanisms rather than from isolated effects. First, the introduction of *CdIn2S4* establishes a favorable conduction-band alignment at the absorber/buffer interface, resulting in improved electron selectivity and an increased effective built-in potential. This enhanced band bending facilitates efficient charge separation and extraction.

Second, the improved interfacial energetics suppress Shockley–Read–Hall recombination by reducing carrier accumulation and trap-assisted recombination at the heterointerface, as quantitatively evidenced by the interface defect density analysis and the higher V_{bi} extracted from the Mott–Schottky measurements. The reduction in recombination losses directly contributes to the observed increase in open-circuit voltage and fill factor.

Third, the optical transparency of *CdIn2S4* minimizes parasitic absorption in the buffer layer, allowing a larger fraction of short-wavelength photons to reach the Sb_2Se_3 absorber. This enhanced photon utilization increases photogeneration and leads to a higher short-circuit current density, consistent with the EQE and absorption analyses.

Together, these electronic and optical improvements act synergistically, producing simultaneous enhancements in V_{oc}, J_{sc}, and FF. The combined effect of optimized band alignment, suppressed interfacial recombination, and reduced parasitic absorption ultimately accounts for the substantial efficiency improvement achieved in the proposed device.

Fig. 4(a), presents the capacitance as a function of frequency for both the reference cell and the proposed cell. This diagram provides valuable insights into the electrical characteristics and the frequency response of the solar cell system, which is crucial for understanding the energy storage capacity and behavior of the cell under varying frequency conditions. Capacitance is a critical parameter in solar cells, as it indicates the ability of the system to store electrical charge in response to frequency pulses. This feature directly affects the solar cell efficiency and its response to changes in frequency in practical operating conditions. In the reference structure, which uses *CdS* as the buffer layer, the capacitance remains relatively constant at low frequencies and then decreases rapidly at higher frequencies. This sharp decrease at higher frequencies indicates energy dissipation and inability to retain charge at high frequencies. In other words, *CdS* due to its weaker dielectric properties compared to *CdIn2S4*, struggles to maintain the stored charges at higher frequencies, leading to reduced solar cell performance in such conditions.

In contrast, the proposed structure with *CdIn2S4* as the buffer layer exhibits a more gradual decrease in capacitance at higher frequencies. This characteristic suggests a better response to high frequencies and greater stability in charge storage. Specifically, *CdIn2S4*, with its optimized dielectric properties, performs significantly better in maintaining charge and reducing energy losses at higher frequencies. This results in improved stability and reduced electrical losses, contributing directly to enhanced solar cell performance. [55,56].

The analysis of the capacitance-frequency curve highlights several key advantages of the proposed structure over the reference structure. Firstly, the proposed structure demonstrates higher capacitance at high

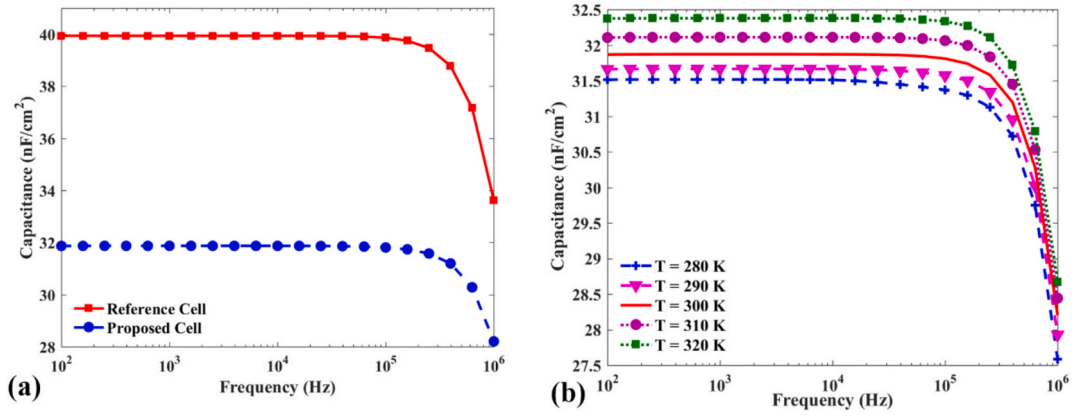

Fig. 4. (a), Capacitance as a function of frequency for the reference and proposed structures (*Sb2Se3*/*CdIn2S4*/*ZnO*/*Al* : *ZnO*). The proposed structure, with *CdIn2S4* as the buffer layer, exhibits better performance at higher frequencies, indicating greater stability in charge storage and reduced energy losses. (b), Capacitance as a function of frequency at different temperatures for the reference and proposed structures. The diagram shows better performance of the proposed structure in response to frequency changes and greater stability in charge storage at higher temperatures and frequencies.

frequencies, reflecting a better response to high-frequency signals and reduced energy dissipation. This improvement in capacitance indicates lower charge losses and increased stability in the system. Furthermore, the more stable capacitance in the proposed structure at higher frequencies leads to enhanced solar cell performance by reducing electrical losses. By using *CdIn2S4* as the buffer layer, the proposed structure offers superior charge retention and reduced energy losses, contributing to the overall improvement in solar cell efficiency compared to *CdS* in the reference structure.

Fig. 4(b), presents the capacitance–frequency (C–f) response of the reference and proposed devices at different operating temperatures ranging from 280 K to 320 K. At lower temperatures (280 K), the devices exhibit relatively high capacitance at low frequencies followed by a rapid decrease at higher frequencies, indicating pronounced capacitive dispersion and limited charge retention under fast alternating signals. As the temperature increases to 290 K and 300 K, the capacitance decay with frequency becomes noticeably more gradual. This behavior reflects improved charge transport dynamics and reduced frequency-dependent losses, leading to a more stable capacitive response. At elevated temperatures (310 K and 320 K), the capacitance remains comparatively higher in the high-frequency regime, suggesting enhanced junction responsiveness and improved charge storage stability. Overall, the temperature-dependent C–f analysis demonstrates that higher operating temperatures lead to reduced capacitive dispersion and lower electrical losses, particularly in the proposed structure. This improved frequency stability at elevated temperatures is consistent with enhanced carrier transport and contributes to the superior electrical performance of the *CdIn2S4*-based device.

The use of *CdIn2S4* as the buffer layer results in a more stable capacitance response at high frequencies compared to the *CdS*-based reference structure. This behavior indicates an improved high-frequency response and more effective charge retention in the proposed device, reflecting reduced frequency-dependent energy losses.

The capacitance–frequency analysis highlights several advantages of the *CdIn2S4*-based architecture, including higher capacitance values in the high-frequency regime and lower capacitive dispersion. These features signify reduced charge loss and enhanced electrical stability, which directly contribute to improved device performance under practical operating conditions. Overall, the superior high-frequency capacitance behavior confirms that $CdIn_2S_4$ effectively mitigates electrical losses and plays a key role in enhancing the efficiency of the proposed solar cell compared to the conventional *CdS* buffer layer.

In Fig. 5(a), the variation of open-circuit voltage (V_{oc}) with temperature for the proposed device is presented. As observed, Voc decreases with increasing temperature, which is a typical behavior in semiconductor solar cells and is primarily attributed to enhanced recombination and reduced quasi-Fermi level splitting at elevated temperatures.

At lower temperatures, reduced thermal activation limits recombination processes and preserves a higher effective built-in potential, leading to improved voltage characteristics. Consequently, the temperature dependence of Voc is governed mainly by recombination dynamics rather than carrier mobility. Fig. 5(b) shows the variation of the short-circuit current density (J_{sc}) with temperature. As observed, J_{sc} exhibits a gradual increase with increasing temperature, which is primarily attributed to enhanced carrier collection efficiency and reduced recombination losses, as thermally activated transport facilitates more effective extraction of photogenerated carriers. In Fig. 5 (c), the fill factor (FF) is analyzed at different temperatures for the proposed structure. It is observed that FF decreases with increasing temperature.

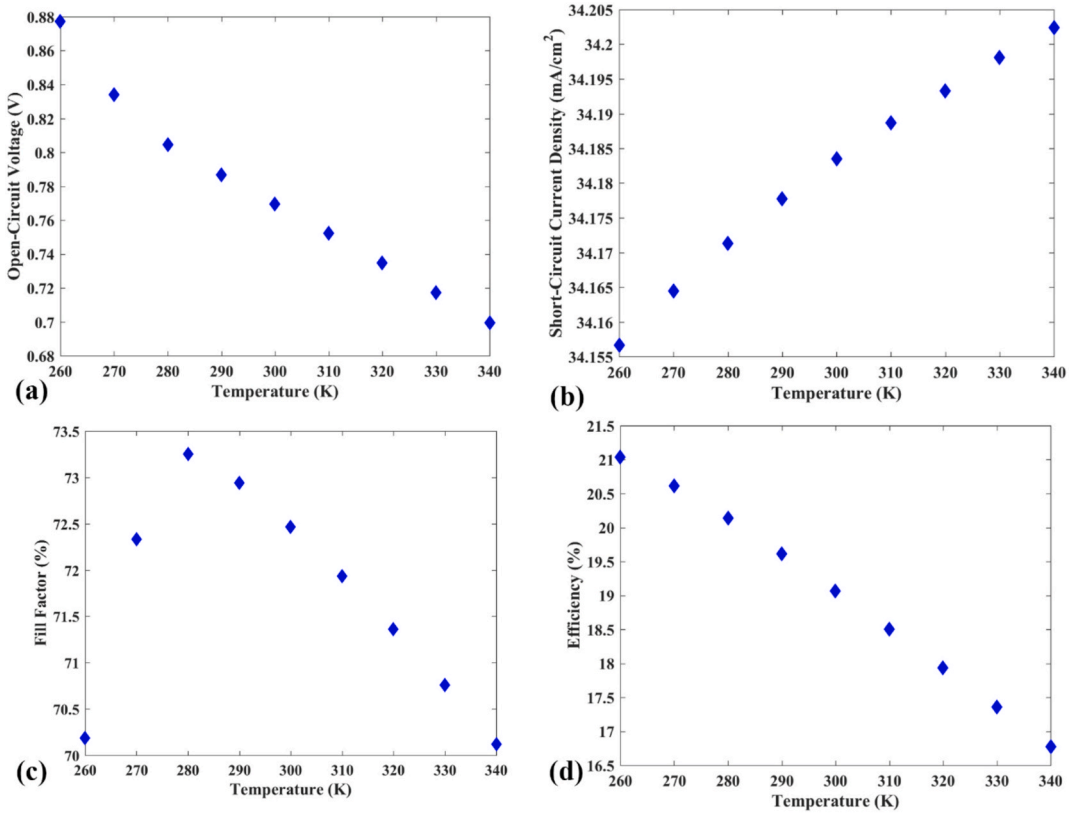

Fig. 5. (a), Variation of open-circuit voltage (V_{oc}) with temperature for the proposed device, showing a decrease at elevated temperatures due to enhanced recombination and reduced effective built-in potential. (b), Temperature dependence of short-circuit current density (J_{sc}), exhibiting a gradual increase with temperature as a result of improved carrier collection and reduced recombination losses. (c), Fill factor (FF) as a function of temperature, indicating increased electrical losses at higher temperatures. (d), Power conversion efficiency (η) versus temperature, showing performance degradation at elevated temperatures due to cumulative thermal losses.

This decrease is due to increased electrical losses and decreased solar cell performance at higher temperatures. In other words, at higher temperatures, electrical losses and defective states at interface layers increase, directly impacting solar cell performance and fill factor. Fig. 5 (d), shows the solar cell efficiency (η) as a function of temperature for the proposed structure. This graph indicates a decrease in η at higher temperatures. Despite the increase in J_{sc}, V_{oc}, and FF at lower temperatures, the increase in energy losses and overall decrease in solar cell performance at higher temperatures leads to a decrease in overall efficiency.

To quantitatively decompose the efficiency improvement, we separate the contributions associated with photocurrent generation/collection (J_{sc}) and recombination-limited voltage (V_{oc}). From the simulated J–V results, J_{sc} increases from 30.87 to 34.18 $mAcm^{-2}$, i.e., $\Delta J_{sc} = +3.31\ mAcm^{-2}$ (≈10.7%), when *CdS* is replaced by $CdIn_2S_4$. This current gain is consistent with the absorption/EQE results, indicating reduced parasitic absorption in the buffer layer and improved utilization of short-wavelength photons.

The voltage improvement is even more pronounced: V_{oc} increases from 0.48 to 0.77 V ($\Delta V_{oc} = +0.29$). At open circuit, the quasi-Fermi level splitting satisfies $\Delta E_F \approx qV_{oc}$; therefore, the proposed structure achieves an additional QFLS of approximately 0.29 eV, reflecting a substantially lower recombination loss. Using the diode approximation $V_{oc} \approx \frac{nkT}{q}\ln\left(\frac{J_{sc}}{J_0}\right)$, the measured ΔV_{oc} implies a large reduction in the effective saturation current J_0 despite only a modest increase in J_{sc}. Quantitatively, the inferred reduction in J_0 is on the order of $10^2 - 10^4$ (depending on the effective ideality factor), which is consistent with suppressed interface SRH recombination and the higher built-in potential extracted from Mott–Schottky analysis.

Overall, the efficiency gain is therefore driven by (i) an optical-current contribution (ΔJ_{sc}) associated with reduced buffer parasitic absorption and enhanced photon delivery to Sb_2Se_3, and (ii) a recombination-voltage contribution (ΔV_{oc}) associated with improved band alignment and reduced interfacial recombination, corroborated by the defect-sensitivity and V_{bi} analyses.

To quantitatively evaluate the role of interfacial defects, the defect density at the *Sb2Se3*/*CdIn2S4* interface was systematically varied from 10^{10} to 10^{14} cm^{-2}. The changes in open-circuit voltage (V_{oc}) as a function of interface defect density between *Sb2Se3* and *CdIn2S4* are illustrated in Fig. 6(a). As seen, V_{oc} decreases with an increase in interface defect density. This decrease is directly attributed to increased carrier recombination at the interface. Interface defects act as recombination centers, which cause a reduction in the internal potential of the solar cell. The Shockley-Read-Hall (SRH) model is used to calculate carrier recombination.

In Fig. 6(b), the short-circuit current density (J_{sc}) as a function of interface defect density between *Sb2Se3* and *CdIn2S4* is presented. The graph clearly shows a decrease in J_{sc} as the interface defect density increases. This behavior is indicative of the detrimental impact that interface defects have on carrier extraction efficiency within the solar cell. At the interface between *Sb2Se3* and *CdIn2S4*, the interface defects act as trap states for the photo-generated carriers. These defects capture electrons and holes, preventing them from reaching the electrodes. As the interface defect density increases, the density of trapped carriers also increases, which leads to a reduction in the overall current collected by the solar cell.

The decrease in J_{sc} with increasing defect density can be attributed to several factors: Firstly, an increased recombination. At higher defect densities, more recombination centers are present at the interface,

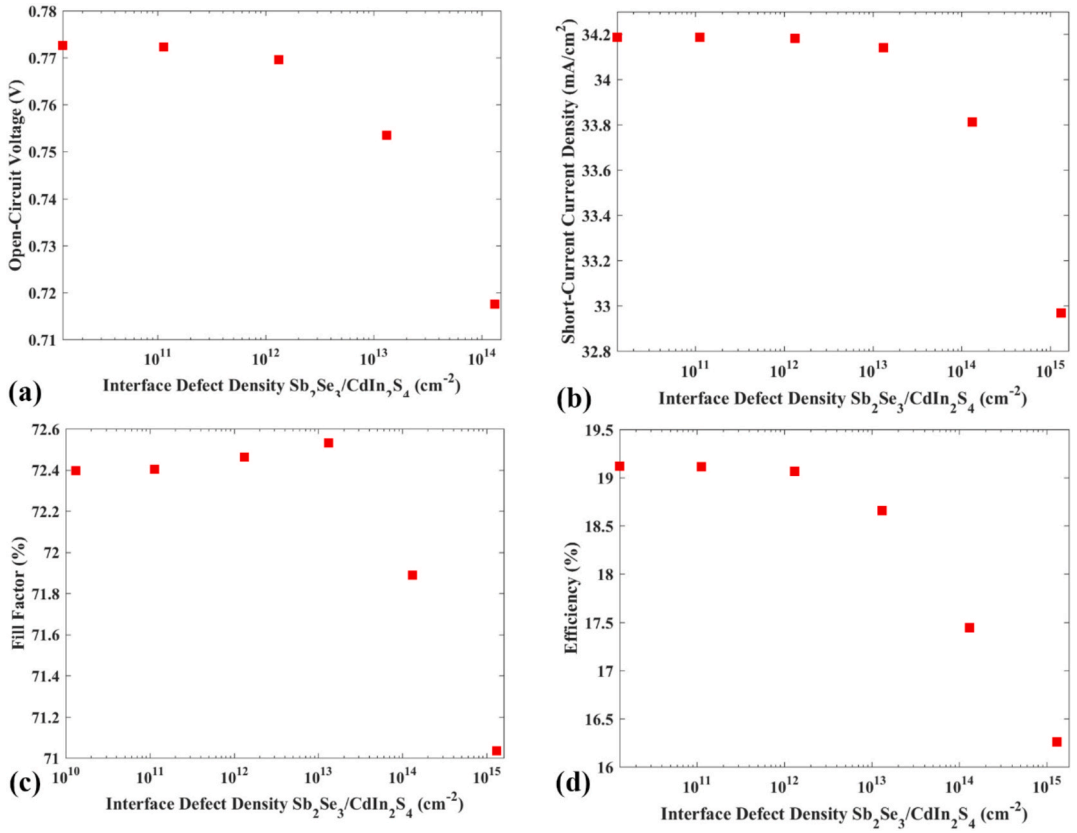

Fig. 6. (a) Open-circuit voltage (V_{oc}) as a function of interface defect density at the *Sb2Se3*/*CdIn2S4* junction, showing a monotonic reduction in V_{oc} due to enhanced Shockley–Read–Hall (SRH) recombination. (b) Short-circuit current density (J_{sc}) versus interface defect density, indicating that elevated Nit increases recombination losses near the heterojunction and suppresses carrier collection. (c) Fill factor (FF) as a function of interface defect density. (d) efficiency (η) variation with interface defect density.

which increases the loss of charge carriers before they can be collected at the electrodes. Secondly, impeded charge transport. Interface defects also disrupt the smooth flow of charge carriers, causing increased resistance at the interface and hindering the effective extraction of charge carriers from the absorber layer. This behavior emphasizes the critical importance of reducing interface defects in solar cell fabrication. By minimizing defects, we can enhance the collection efficiency of photo-generated carriers and thus increase the short-circuit current density (J_{sc}), which ultimately improves the overall performance of the solar cell.

In Fig. 6(c), the changes in fill factor (FF) as a function of interface defect density between *Sb2Se3* and *CdIn2S4* are presented. As seen in the graph, FF decreases with increasing interface defect density. This decrease is directly attributed to increased carrier recombination, higher internal resistance, and lower energy conversion efficiency at the interface. Fill factor (FF) is a critical parameter that indicates the efficiency of charge collection and the overall performance of the solar cell. It is essentially the ratio of the maximum output power to the product of open-circuit voltage (V_{oc}) and short-circuit current density (J_{sc}). The reduction in FF with increasing defect density suggests a loss in the solar cell's ability to effectively convert absorbed photons into usable electrical power. As interface defect density increases, carrier recombination becomes more significant at the interface, leading to lower charge collection efficiency. Also, the increased internal resistance due to the defects causes more energy losses, reducing the efficiency of the solar cell. Overall, the fill factor decreases, indicating a drop in solar cell performance. Finally, in Fig. 6(d), the relationship between solar cell efficiency (η) and interface defect density between Sb_2Se_3 and *CdIn2S4* is presented. As seen in the graph, efficiency (η) decreases with increasing interface defect density. This decrease is directly attributed to higher carrier recombination rates and increased energy losses at the interface. The interface defects at the boundary between *Sb2Se3* and *CdIn2S4* act as recombination centers for the photo-generated carriers, leading to reduced carrier collection efficiency and increased energy losses. These defects introduce energy states within the bandgap, trapping charge carriers and preventing their movement toward the electrodes. These carrier recombination processes directly result in the decrease of open-circuit voltage (V_{oc}) and short-circuit current density (J_{sc}), which consequently impacts the solar cell efficiency (η). As interface defect density increases, the interface defects lead to higher carrier recombination, which in turn causes higher energy losses. These increased energy losses, arising from reduced carrier separation efficiency and lower power output, result in a decrease in solar cell efficiency. Therefore, interface defect density plays a crucial role in determining the performance of the solar cell and significantly impacts the overall cell efficiency.

As result at low interface defect densities ($\leq 10^{11}\,cm^{-2}$), the device exhibits stable photovoltaic parameters, indicating efficient charge separation and minimal interfacial recombination. However, as the defect density increases beyond $10^{12}\,cm^{-2}$, all performance metrics deteriorate markedly. This degradation is primarily attributed to enhanced Shockley–Read–Hall recombination at the heterointerface, which reduces carrier lifetime and limits charge extraction.

The impact of interface defects is particularly pronounced in the open-circuit voltage and fill factor, reflecting increased recombination losses and degraded junction quality. As a result, the power conversion efficiency decreases sharply at high defect densities, demonstrating the critical importance of interface passivation for achieving high-performance *Sb2Se3*-based devices.

Importantly, this trend is consistent with the built-in potential extracted from the Mott–Schottky analysis. Lower interface defect densities lead to improved band bending and a higher effective built-in potential, whereas increased defect density induces interfacial charge trapping and partial Fermi-level pinning, resulting in a reduced V_{bi}. This correlation confirms that the observed performance enhancement in the proposed structure is directly linked to the reduced interface defect density at the *Sb2Se3*/*CdIn2S4* junction.

In Fig. 7(a), the Mott-Schottky plot is presented, comparing the interface defect density of two solar cell structures: $Sb_2Se_3/CdIn_2S_4$ (proposed cell) and *Sb2Se3*/*CdS* (reference cell). The plot shows the inverse of the capacitance (C^{-2}) as a function of voltage (V), which is commonly used to analyze the built-in potential and carrier density within the semiconductor materials. The slope of the line in this plot is crucial for understanding the carrier distribution in the depletion region, which is influenced by the interface properties and defect densities of the materials. From the graph, it is clear that the built-in potential for the *Sb2Se3*/*CdIn2S4* structure is 1.05 V, whereas for the *Sb2Se3*/*CdS* structure, it is only 0.78 V. This significant difference in built-in potential is indicative of the improved band alignment and charge separation efficiency in the proposed structure, highlighting the advantages of using *CdIn2S4* as the buffer layer instead of CdS. The higher built-in potential in the proposed structure leads to a stronger built-in electric field at the interface, which aids in more efficient carrier separation and prevents recombination losses.

The Mott-Schottky analysis reveals that the *Sb2Se3*/*CdIn2S4* interface exhibits less carrier recombination and better charge transport compared to the *Sb2Se3*/*CdS* interface. This is because the *CdIn2S4* layer, with its optimized type-II band alignment and lower defect density, helps reduce the trap-assisted recombination that is common in CdS. The increased the built-in potential in the proposed structure is a direct consequence of this improvement, which contributes to the higher overall efficiency of the *Sb2Se3*/*CdIn2S4* solar cell. Furthermore, the interface defect density plays a critical role in determining the performance of the solar cell. As shown in the plot, higher defect densities at the interface result in a lower built-in potential, which leads to reduced efficiency due to increased carrier recombination and lower charge collection efficiency. Therefore, the results highlight the importance of minimizing defects at the interface to enhance the overall performance of thin-film solar cells.

The Mott-Schottky plot illustrates the significant advantage of the *Sb2Se3*/*CdIn2S4* structure over the *Sb2Se3*/*CdS* structure in terms of the built-in potential, indicating better charge separation efficiency and reduced recombination losses. This improvement is attributed to the better band alignment and lower defect density at the *Sb2Se3*/*CdIn2S4* interface, making it a more effective buffer layer for high-performance solar cells.

Fig. 7(b), presents the Nyquist impedance spectra of the reference *Sb2Se3*/*CdS* device and the proposed *Sb2Se3*/*CdIn2S4* device. The spectra are plotted as the imaginary component of the impedance (−Im Z) versus the real component (Re Z), providing insight into recombination-related resistive processes and capacitive response within the devices under small-signal perturbation.

In both devices, the Nyquist plots exhibit a dominant semicircular feature in the high-to-intermediate frequency range, which can be associated within the adopted equivalent-circuit framework with an effective recombination or charge-transfer resistance in parallel with a junction capacitance. It should be noted that the absolute value of this resistance depends on the selected circuit model and frequency window; therefore, the analysis focuses on relative differences between the two device architectures rather than absolute impedance values.

Compared to the reference *Sb2Se3*/*CdS* device, the proposed *Sb2Se3*/*CdIn2S4* structure exhibits a larger semicircle diameter, indicating a higher effective recombination resistance. This trend suggests suppressed interfacial recombination and improved junction quality in the proposed device. The increased recombination resistance is consistent with the improved band alignment and reduced interface defect density at the *Sb2Se3*/*CdIn2S4* heterointerface, as independently supported by the defect-sensitivity analysis and the enhanced built-in potential extracted from Mott–Schottky measurements.

In contrast, the smaller semicircle observed for the *Sb2Se3*/*CdS* de-

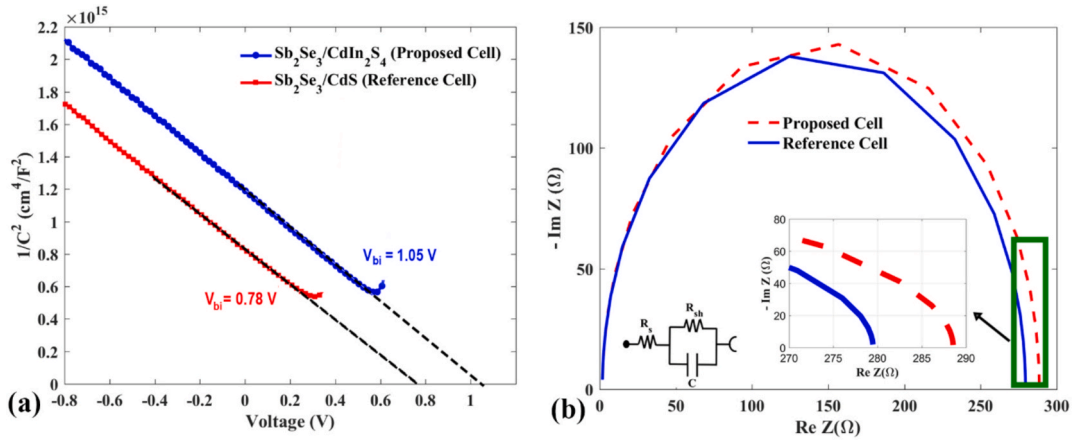

Fig. 7. (a), Mott-Schottky Plot for the Proposed and Reference Cells. (b), Nyquist Plot for the Proposed and Reference Cells.

vice indicates lower recombination resistance, reflecting stronger recombination activity at the absorber/buffer interface. This behavior is consistent with the less favorable conduction-band alignment and higher sensitivity to interface defects in the CdS-based junction.

Overall, the comparative Nyquist analysis supports the conclusion that replacing *CdS* with *CdIn2S4* improves interfacial electronic quality by increasing the effective recombination resistance and stabilizing the junction response. These impedance trends align with the observed enhancements in open-circuit voltage, fill factor, and overall device efficiency, reinforcing the role of interface optimization in the proposed architecture.

To further contextualize the simulated 19.06% efficiency, Table 2, compares the proposed *Sb2Se3/CdIn2S4* device with representative Sb_2Se_3 architectures employing alternative buffer layers reported in the literature, including *Zn(O,S)*, *TiO2*-based buffers/interlayers, and other *Cd*-free chalcogenide/oxide buffers. In general, *Zn(O,S)* is frequently adopted because its conduction-band offset can be tuned by adjusting the *S/O* ratio; however, its performance is often sensitive to composition uniformity, processing control, and interface defects. *TiO2* interlayers can provide improved electron selectivity and act as a recombination barrier, yet they may introduce transport limitations or interface states depending on deposition and phase, and their optical/electrical impact strongly depends on thickness and defect chemistry.

In comparison,*CdIn2S4* offers a distinctive combination of (i) reduced parasitic absorption in the buffer region, enabling improved short-wavelength photon utilization, and (ii) favorable band alignment at the *Sb2Se3*/buffer interface, which promotes efficient electron extraction while suppressing interfacial recombination. These advantages are consistent with the observed improvements in the EQE response, the reduced defect sensitivity at the heterointerface, and the increased built-in potential derived from capacitance-based analyses. The overall outcome is a simultaneous enhancement of J_{sc}, V_{oc}, and FF, yielding the high simulated PCE reported in this work.

From a practical perspective, it is also important to acknowledge material-sustainability trade-offs. Indium is less abundant than several oxide alternatives (e.g., *ZnO* −, *SnO2*-based buffers), and its large-scale use can raise supply-chain considerations. However, in this architecture *CdIn2S4* functions as an ultrathin buffer layer, so the absolute indium consumption is relatively small compared to absorber or TCO layers. In addition, the benefits demonstrated here can guide future device design by informing buffer thickness minimization and by providing design rules that may also be transferable to other Cd-free buffer candidates. Therefore, while *CdIn2S4* is shown to be a highly effective buffer for performance optimization, continued evaluation of Cd-free, earth-abundant alternatives remains essential for scalable deployment.

While the proposed *Sb2Se3/CdIn2S4* architecture demonstrates a substantial efficiency enhancement in simulation, it is important to recognize that these results represent an idealized upper-bound scenario. In practical implementations, the achievable performance will depend critically on the structural quality of the *CdIn2S4* buffer layer, including grain morphology, defect density, and thickness uniformity, which are strongly influenced by the chosen deposition technique. Moreover, the chemical stability and interfacial integrity of the *Sb2Se3/CdIn2S4* heterojunction under thermal processing and long-term operation may introduce additional recombination pathways that are not fully captured in idealized simulations.

In addition, non-ideal carrier transport across the buffer layer or imperfect interface formation may increase the series resistance, thereby reduce the fill factor and limit the experimentally achievable efficiency. Consequently, the reported 19.06% efficiency should be interpreted as a theoretical performance ceiling that highlights the potential of *CdIn2S4* as an alternative buffer layer, rather than as an immediately attainable experimental benchmark. Nonetheless, the insights gained from this study provide valuable design guidance for future experimental efforts aimed at interface optimization and performance enhancement in Sb_2Se_3-based thin-film solar cells.

Table 2
Comparison of V_{oc}, J_{sc}, Fill Factor (FF), and Efficiency (η) values from both experimental and simulation studies. The data includes results from several research cases, showing the performance enhancement achieved in this work with the proposed *Sb2Se3/CdIn2S4* solar cell structure.

Research Case	V_{oc}(V)	$J_{sc}(mA/cm^2)$	FF (%)	η(%)	Reference
Experimental	0.57	10.23	55.34	3.21	[23]
Experimental	0.39	26.25	57.83	5.94	[57]
Experimental	0.42	25.49	59.34	6.52	[24]
Experimental	0.48	30.86	67.19	10.12	[5]
Simulation	0.77	34.18	72.16	19.06	This work

5. Conclusion

In this study, the performance of *Sb2Se3* solar cells with the *CdIn2S4* buffer layer as an alternative to CdS was evaluated. The simulation results showed a significant increase in solar cell efficiency, from 10.12% in the reference structure to 19.06% in the proposed structure. This improvement is primarily attributed to the optimized band alignment between *Sb2Se3* and *CdIn2S4*, which reduces energy losses and enhances charge separation. Additionally, *CdIn2S4*, with its wider bandgap and lower photon absorption in the visible range, allows more photons to reach the absorber layer, which leads to an increase in short-circuit current density (J_{sc}). Furthermore, the reduced charge-transfer resistance in the proposed cell indicates more efficient interfacial charge transfer and suppressed recombination losses. This research demon-

strates that *CdIn2S4* as a buffer layer not only improves efficiency and reduces energy losses, but also offers better chemical compatibility and environmental sustainability, making it a viable and scalable option for thin-film solar cells. Overall, replacing CdS with *CdIn2S4* significantly enhances the performance and efficiency of the solar cell, and the proposed structure could lead to the development of more efficient and stable solar cells in the future.

6. Ethical Approval Statement

The authors confirm that the submitted paper has not been submitted to any other journal and that this version is original and has not been published elsewhere. Additionally, all listed authors affirm the integrity of the study, data, information, and analyses, ensuring that no manipulations have been made. Furthermore, we confirm that no other individuals meet the authorship criteria for this paper beyond those listed as authors.

7. Declarations

AI tools were used to improve the English content of this paper.

CRediT authorship contribution statement

Danial Keighobadi: Writing – original draft, Software, Investigation, Data curation. **Mehdi Mousavi-Kamazani:** Validation, Supervision, Data curation, Conceptualization. **Mohammad Danaie:** Writing – review & editing, Supervision, Project administration, Formal analysis, Conceptualization.

Funding

The authors declare that no funds, grants, or financial support were received for the preparation of this manuscript.

Declaration of competing interest

The authors declare that they have no known competing financial interests or personal relationships that could have appeared to influence the work reported in this paper.

Data availability

Data will be made available on request.

References

[1] C. Chen, K. Li, J. Tang, Ten years of Sb_2Se_3 thin film solar cells, Sol. RRL 6 (7) (2022) 2200094.
[2] N. Kant, P. Singh, Review of next generation photovoltaic solar cell technology and comparative materialistic development, Mater. Today Proc. 56 (2022) 3460–3470.
[3] M. Jost, et al., Perovskite/CIGS tandem solar cells: from certified 24.2% toward 30% and beyond, ACS Energy Lett. 7 (4) (2022) 1298–1307.
[4] Y. Gong, et al., Elemental de-mixing-induced epitaxial kesterite/CdS interface enabling 13%-efficiency kesterite solar cells, Nat. Energy 7 (10) (2022) 966–977.
[5] Z. Duan, et al., Sb2Se3 thin-film solar cells exceeding 10% power conversion efficiency enabled by injection vapor deposition technology, Adv. Mater. 34 (30) (2022) 2202969.
[6] N. Nikfar, N. Memarian, Theoretical study on the effect of electron transport layer parameters on the functionality of double-cation perovskite solar cells, Optik 258 (2022) 168932.
[7] H. Cai, et al., Interfacial engineering towards enhanced photovoltaic performance of Sb_2Se_3 solar cell, Adv. Funct. Mater. 32 (46) (2022) 2208243.
[8] A.S. Al-Ezzi, M.N.M. Ansari, Photovoltaic solar cells: a review, Appl. Syst. Innov. 5 (4) (2022) 67.
[9] M. Minbashi, et al., Simulation of high efficiency SnS-based solar cells with SCAPS, Sol. Energy 176 (2018) 520–525.
[10] A. Ait Abdelkadir, et al., Numerical simulation and optimization of n-Al-ZnO/n-CdS/p-CZTSe/p-NiO (HTL)/Mo solar cell system using SCAPS-1D, Results Opt. 8 (2022) 100257.
[11] T. Wu, et al., The main progress of perovskite solar cells in 2020–2021, Nano-Micro Letters 13 (1) (2021) 152.
[12] G. Wu, et al., Study of antimony selenide hole-transport material for Mo/Sb_2Se_3/$MAPbI_3$/C60/GZO/Ag heterojunction planar solar cells, Surf. Coat. Technol. 405 (2021) 126550.
[13] T.S. Natarajan, R.J. Tayade, Direct dual $CaIn_2S_4/Bi_2WO_6$ semiconductor nanocomposites with efficient inter-cross-sectional charge carrier transfer for enhanced visible light photocatalysis, J. Nanopart. Res. 23 (6) (2021) 127.
[14] U. Daraz, et al., Fabrication, characterization, and photocatalytic performance of ternary cadmium chalcogenides $CdIn_2S_4$ and Cd_7. $23Zn_2$. 77S10-ZnS thin films, Main Group Met. Chem. 44 (1) (2021) 39–50.
[15] M.A. Hamza, G.F. Metha, C.J. Shearer, Recent advances and future directions of CdIn 2 S 4-based photocatalysts: properties, synthesis, and modifications for energy and environmental applications, J. Mater. Chem. A 13 (27) (2025) 21292–21351.
[16] Y. Seminovski, et al., Band gap control via tuning of inversion degree in CdIn2S4 spinel, Appl. Phys. Lett. 100 (10) (2012).
[17] G. Yadav, M. Ahmaruzzaman, CdIn2S4-based advanced composite materials: structure, properties, and applications in environment and energy–a concise review, Inorg. Nano-Metal Chem. 55 (2) (2025) 122–136.
[18] A. Wang, et al., Hydrogen-enhanced carrier collection enabling wide-bandgap Cd-free Cu_2ZnSnS_4 solar cells with 11.4% certified efficiency, Nat. Energy 10 (2) (2025) 255–265.
[19] Y. Luo, et al., Rapid thermal-driven crystal growth and defect suppression in antimony selenide thin film for efficient solar cells, Small 21 (1) (2025) 2403051.
[20] N. Ahmad, J. Yuan, Y. Zou, One more step towards better stability of non-fullerene organic solar cells: advances, challenges, future perspective, and era of artificial intelligence, Energ. Environ. Sci. (2025).
[21] N. Ahmad, et al., Data-mining and machine learning based search for optimal materials for perovskite and organic solar cells, Sol. Energy 287 (2025) 113223.
[22] M. Minbashi, et al., Comparison of theoretical and experimental results for band-gap-graded CZTSSe solar cell, Curr. Appl Phys. 17 (10) (2017) 1238–1243.
[23] H. Deng, et al., Efficient and stable TiO_2/Sb_2S_3 planar solar cells from absorber crystallization and Se-atmosphere annealing, Mater. Today Energy 3 (2017) 15–23.
[24] C. Chen, et al., 6.5% certified efficiency Sb_2Se_3 solar cells using PbS colloidal quantum dot film as hole-transporting layer, ACS Energy Lett. 2 (9) (2017) 2125–2132.
[25] Choubey, P., A. Oudhia, and R. Dewangan, A review: Solar cell current scenario and future trends. Recent Research in Science and Technology, 2012. **4**(8).
[26] N. Asim, et al., A review on the role of materials science in solar cells, Renew. Sustain. Energy Rev. 16 (8) (2012) 5834–5847.
[27] Z.-S. Wang, et al., Significant influence of TiO2 photoelectrode morphology on the energy conversion efficiency of N719 dye-sensitized solar cell, Coord. Chem. Rev. 248 (13–14) (2004) 1381–1389.
[28] M.K. Omrani, et al., Improve the performance of CZTSSe solar cells by applying a SnS BSF layer, Solid State Electron. 141 (2018) 50–57.
[29] T. Kirchartz, U. Rau, What makes a good solar cell? Adv. Energy Mater. 8 (28) (2018) 1703385.
[30] Rong, Y., et al., Challenges for commercializing perovskite solar cells. Science, 2018. **361**(6408): p. eaat8235.
[31] S. Xu, et al., Facile synthesis of novel CaIn2S4/ZnIn2S4 composites with efficient performance for photocatalytic reduction of Cr (VI) under simulated sunlight irradiation, Nanomaterials 8 (7) (2018) 472.
[32] X. Wang, et al., Interfacial engineering for high efficiency solution processed Sb_2Se_3 solar cells, Sol. Energy Mater. Sol. Cells 189 (2019) 5–10.
[33] N. Ahmad, et al., Cadmium-free kesterite thin-film solar cells with high efficiency approaching 12%, Adv. Sci. 10 (26) (2023) 2302869.
[34] I. Gharibshahian, A.A. Orouji, S. Sharbati, Towards high efficiency Cd-Free Sb_2Se_3 solar cells by the band alignment optimization, Sol. Energy Mater. Sol. Cells 212 (2020) 110581.
[35] I. Gharibshahian, A.A. Orouji, S. Sharbati, Alternative buffer layers in Sb_2Se_3 thin-film solar cells to reduce open-circuit voltage offset, Sol. Energy 202 (2020) 294–303.
[36] Z.-Q. Li, M. Ni, X.-D. Feng, Simulation of the Sb_2Se_3 solar cell with a hole transport layer, Mater. Res. Express 7 (1) (2020) 016416.
[37] M. Al-Hattab, et al., Numerical simulation of a new heterostructure CIGS/GaSe solar cell system using SCAPS-1D software, Sol. Energy 227 (2021) 13–22.
[38] I. Gharibshahian, A.A. Orouji, S. Sharbati, Efficient Sb2 (S, Se) 3/Zn (O, S) solar cells with high open-circuit voltage by controlling sulfur content in the absorber-buffer layers, Sol. Energy 227 (2021) 606–615.
[39] X. Jin, et al., Controllable solution-phase epitaxial growth of Q1D Sb2 (S, Se) 3/CdS heterojunction solar cell with 9.2% efficiency, Adv. Mater. 33 (44) (2021) 2104346.
[40] K. Maurya, V. Singh, Sb_2Se_3 versus Sb_2S_3 solar cell: a numerical simulation, Sol. Energy 228 (2021) 540–549.
[41] Geravand, A., S. Sharbati, and M. Danaie. Optimize parameters of new fabricated n-CdTe/p-CdTe solar cell. in 2017 Iranian Conference on Electrical Engineering (ICEE). 2017. IEEE.
[42] H. Zai, et al., Wafer-scale monolayer MoS_2 film integration for stable, efficient perovskite solar cells, Science 387 (6730) (2025) 186–192.
[43] B. Zhang, et al., Recent advances in tin halide perovskite solar cells: a critical review, J. Mater. Chem. A 13 (37) (2025) 30708–30754.
[44] D. Xu, et al., Record-efficiency inverted $CsPbI_3$ perovskite solar cells enabled by rearrangement and hydrophilic modification of SAMs, Adv. Funct. Mater. 35 (2) (2025) 2412946.
[45] J. Xin, et al., Recent advances in polymorphism of organic solar cells, Small 21 (6) (2025) 2409411.
[46] J.P. Tiwari, Flexible perovskite solar cells: a futuristic iots powering solar cell technology, short review, Small Methods 9 (1) (2025) 2400624.

[47] G. Tang, et al., A Review on recent advances in flexible perovskite solar cells, Sol. RRL 9 (5) (2025) 2400844.
[48] J. Tan, et al., Research and development of modification strategies based on all inorganic perovskite solar cells, Nano Energy (2025) 110815.
[49] Pu, D., et al., Imprisoning 2H intermediate phases in blade-coated wide-bandgap perovskites for efficient all-perovskite tandem solar cells. Science Advances, 2025. **11**(34): p. eady3621.
[50] A. Miglani, S.B. Ogale, O.S. Game, Architectural innovations in perovskite solar cells, Small 21 (15) (2025) 2411355.
[51] M.H. Miah, et al., Lead-free alternatives and toxicity mitigation strategies for sustainable perovskite solar cells: a critical review, Mater. Adv. 6 (9) (2025) 2718–2752.
[52] Z. Luo, et al., albendazole passivation in inverted wide-bandgap perovskite solar cells toward efficient perovskite/$CuInGaSe_2$ tandem photovoltaics, Adv. Mater. 37 (41) (2025) e05597.
[53] V.C. Karade, et al., Opportunities and challenges for emerging inorganic chalcogenide–silicon tandem solar cells, Energ. Environ. Sci. 18 (14) (2025) 6899–6933.
[54] N. Chawki, et al., Efficacy analysis of BaZrS3-based perovskite solar cells: investigated through a numerical simulation, Adv. Mater. Process. Technol. 11 (1) (2025) 389–402.
[55] Y. An, et al., Balancing carrier transport in interconnection layer for efficient perovskite/organic tandem solar cells, Nat. Commun. 16 (1) (2025) 1–11.
[56] W. Akram, et al., A review of life cycle assessment and sustainability analysis of perovskite/Si tandem solar cells, RSC Sustainability 3 (1) (2025) 21–36.
[57] L. Wang, et al., Stable 6%-efficient Sb2Se3 solar cells with a ZnO buffer layer, Nat. Energy 2 (4) (2017) 1–9.